

Plasma density gradients at the edge of polar ionospheric holes: The ~~presence and~~ absence of phase scintillation

Luke A. Jenner,^[1] Alan G. Wood^[1], Gareth D. Dorrian^[1], Kjellmar Oksavik^[2, 3], Timothy K. Yeoman^[4], Alexandra R. Fogg^[4], and Anthea J. Coster^[5]

^[1] School of Science & Technology, Nottingham Trent University, Nottingham, UK.

^[2] Birkeland Centre for Space Science, Department of Physics and Technology, University of Bergen, Bergen, Norway

^[3] Arctic Geophysics, University Centre in Svalbard, Longyearbyen, Norway

^[4] Department of Physics and Astronomy, University of Leicester, Leicester, UK.

^[5] MIT Haystack Observatory, Massachusetts, USA.

Abstract

Formatted: Right

Polar holes were observed in the high-latitude ionosphere during a series of multi-instrument case studies close to the northern hemisphere winter solstice in 2014 and 2015. These holes were observed during geomagnetically quiet conditions and under a range of solar activities using the European Incoherent Scatter Scientific Association (EISCAT) Svalbard Radar (ESR) and measurements from Global Navigational Satellite System (GNSS) ~~satellite receivers~~ receivers. Steep electron density gradients have been associated with phase scintillation in previous studies, however, no enhanced scintillation was detected within the electron density gradients at these boundaries. It is suggested that the lack of phase scintillation may be due to low plasma density levels and a lack of intense particle precipitation. It may be that both significant electron density gradients and that plasma density levels above a certain threshold are required for scintillation to occur.

27 Introduction

28 The F-region ionosphere is a weakly ionised plasma in the Earth's atmosphere extending from
29 an altitude of ~150 to ~500 km, above which it merges with Earth's plasmasphere. Large-scale
30 plasma structures with a horizontal extent of tens to hundreds of km are routinely observed
31 in the F-region high-latitude ionosphere (Tsunoda, 1988). One type of structure commonly
32 observed are polar cap patches, also referred to as patches, which are enhancements of
33 plasma density with at least twice the background value and have a horizontal spatial extent
34 of 100 km or greater (Crowley, 1996). Buchau et al. (1983) observed such patches of enhanced
35 ionisation drifting antisunward with the background plasma flow in the central region of the
36 polar cap at Thule, Greenland (77.5° N, 69.2° W; 85.4° MLAT, 32.4° MLON). The patch densities
37 were larger than could be produced due to the observed flux of precipitating particles, and it
38 was concluded that the patches were not produced locally by precipitation. Weber et al.
39 (1984) suggested that the patches were produced on the dayside at auroral or subauroral
40 latitudes and then convected antisunward to higher, polar latitudes. A comparison of average
41 maps of the electron density and high-latitude convection pattern suggested that solar-
42 produced plasma was drawn into the polar cap as a continuous density enhancement known
43 as the Tongue-of-Ionisation (TOI) (Foster et al., 1984). Several mechanisms have been
44 proposed to break a TOI into a series of patches, including variations in the high-latitude
45 convection pattern moving flux tubes in and out of sunlight (Anderson et al., 1988), expansion
46 and contraction of the high-latitude convection pattern in response to transient bursts of
47 reconnection drawing in plasma from different latitudes (Cowley and Lockwood, 1992;
48 Lockwood and Carlson, 1992; Carlson et al., 2002, 2004, 2006), variations in the y-component
49 of the Interplanetary Magnetic Field (IMF) drawing in plasma from different magnetic local
50 times (MLT) (Sojka et al., 1993), variation of the z-component of the IMF altering whether
51 plasma could be drawn in to the polar cap (Valladares et al., 1998), erosion of plasma densities
52 due to enhanced recombination during a flow channel event (Rodger et al., 1994; Valladares
53 et al., 1994), and modification of the density of the photoionised plasma transported into the
54 polar cap by particle precipitation (Walker et al., 1999; Millward et al., 1999). Patches have
55 been observed travelling thousands of kilometres across the polar regions (Weber, 1986;
56 Oksavik et al., 2010; Nishimura et al., 2014), and are primarily associated with times when the
57 z-component of the IMF is negative (Buchau and Reinisch, 1991).

Blobs are also plasma density enhancements, however, unlike patches, they occur outside the polar cap. They are further categorised into boundary blobs, subauroral blobs, and auroral blobs (Rino, 1983; Jin et al., 2016). Boundary blobs are found near the equatorward auroral boundary, neighbouring the ionospheric trough's poleward wall. Parkinson et al. (2002) observed patches leaving the polar cap, slowing in the antisunward direction and then beginning to move zonally. It was suggested that these patches would form boundary blobs, and this was later confirmed by Pryse et al. (2006) who compared the plasma density in a polar cap patch to that within a boundary blob which the patch subsequently formed. Subauroral blobs have a similar appearance to boundary blobs, however, they are found in the ionospheric trough. Auroral blobs are found within the auroral oval and seem to be longitudinally restricted. The most likely mechanism for their creation is particle precipitation (Jones et al., 1997).

Not all ionospheric structures are enhancements of the background plasma; polar ionospheric holes are regions of low plasma density. Brinton et al. (1978) observed a depletion of this kind under conditions of low solar activity ($F_{10.7}=71$ sfu) and low magnetic activity ($K_p = 2$). This depletion was also associated with a minimum of electron temperatures, indicating the absence of local particle precipitation. Polar holes are generally located between 21 and 06 MLT and 70° - 80° magnetic latitude and typically have steep plasma density gradients at their boundaries. They are believed to be produced when plasma in the high-latitude convection pattern circulates in perpetual darkness. Plasma loss by recombination in the absence of a plasma source causes density levels to drop. This idea is supported by the conditions under which polar holes have generally been observed, namely quiet geomagnetic activity (K_p 2 or less) when the contribution to the plasma densities from particle precipitation will be low (Brinton et al., 1978). The electron densities inside of the polar holes are seen to reach a minimum in the range of 10^8 - 10^{11} electrons·m⁻³ (Obara and Oya, 1989, Benson and Grebowsky, 2001) and, while there is variation between holes, inside of a singular polar hole the density level is very consistent.

Smaller scale structures can arise at steep plasma density gradients due to instability processes such as the gradient-drift instability (GDI) (Keskinen and Ossakow, 1983) and the velocity shear driven instability (Kelvin-Helmholtz instability, KHI). Carlson et al. (2008) proposed and that the real process involves both mechanisms acting on different time scales.

The smaller scale (tens of meters to tens of kilometers) plasma density structures that arise cause variations in the refractive index of the ionosphere. As a GNSS signal passes through this region, refraction and/or diffraction of the radio wave causes fluctuations in the phase and amplitude of the signal. Ionospheric scintillation is the rapid fluctuation of the received signal which can disrupt applications using GNSS, as thoroughly reviewed by Hapgood (2017).

Since the second world war, large numbers of studies have shown the effect of ionospheric irregularities on radio signals, as reviewed by Aarons (1982). The morphology of these irregularities has been extensively studied at high-latitudes (e.g. Kersley, 1972), together with the effects upon the propagation of radio signals in this region (e.g. Kersley et al., 1995).

More recently studies have focussed on Global Navigation Satellite System (GNSS) frequencies, where scintillation poses a substantial threat to the integrity, availability and accuracy of GNSS positioning, leading to positioning errors and service outages due to signal tracking problems at the GNSS receiver. A direct connection between gradients in the Total Electron Content (TEC) at the edge of a plasma stream with both phase and amplitude scintillation has been observed (Mitchell et al., 2005) and plasma structuring caused by auroral precipitation has been linked to the loss of signal lock by a GNSS receiver (Elmas et al., 2011; Smith et al., 2008; Oksavik et al., 2015). A statistical study has shown an agreement between both phase and amplitude scintillation with the asymmetric distribution of polar cap patches around magnetic midnight (Spogli et al., 2009) and that auroral emissions correlate with GNSS signal phase scintillation (Kinrade et al., 2013; van der Meeren et al., 2015). Phase and amplitude scintillation can be associated with the larger spatial structures associated with polar cap patches (Alfonsi et al., 2011). The climatology of ionospheric scintillation at polar latitudes in the northern hemisphere was determined over almost two solar cycles, and the dependence upon solar cycle, geomagnetic activity and solar wind conditions was shown by De Francheschi et al. (2019). Phase scintillation is usually the dominant process at high latitudes (Spogli et al., 2009; Prikryl et al., 2015) and this is the focus of the present study.

Phase scintillation is commonly quantified by the standard deviation of the signal phase, σ_ϕ , which is usually computed across 60 seconds. The refractive component of the signal is

usually assumed to be slowly varying and associated with frequencies of less than 0.1 Hz. Therefore, by only considering frequencies greater than 0.1 Hz, the diffractive effects (usually referred to as scintillation) can be distinguished (Fremouw et al., 1978). However, the 0.1 Hz cutoff can give spurious observations of phase scintillation as a result of erroneous data detrending (Forte and Radicella, 2002). When a GNSS satellite is observed at low elevation angles the σ_ϕ index cannot distinguish between phase scintillation and background noise for weak to moderate phase scintillation (Forte, 2005). Wang et al. (2018) showed that rapid variations in the phase of a trans-ionospheric signal can arise as a result of plasma structures moving rapidly relative to an observer at ground level, and so can give the appearance of phase scintillation. Rapid changes in the spatial distribution of electron density can also introduce similar effects as the GNSS satellite-to-receiver ray path can sweep through these irregularities at high speed, resulting in high-frequency refractive variations (McCaffrey and Jayachandran, 2019).

The presence or absence of scintillation effects on trans-ionospheric radio signals have been extensively studied for electron density enhancements in the high-latitude ionosphere, but the effect of the steep plasma density gradients at the edge of depletions, such as polar holes are not as extensively studied. The purpose of this paper is to report on the effects of such steep density gradients on GNSS signals, observed in three multi-instrument case studies close to winter solstice.

Instrumentation

The European Incoherent Scatter Scientific Association (EISCAT) operates the EISCAT Svalbard Radar (ESR) at Longyearbyen (78.2° N, 16.0° E; 15.2° MLAT, 112.9° MLON) on Svalbard (Wannberg et al., 1997). The site consists of two antennas, a 32-meter parabolic dish and a 42-meter parabolic dish. The 42 m dish is fixed along the direction of the local geomagnetic field lines (azimuth -179°; elevation 81.6°), while the 32 m dish is steerable in both azimuth and elevation. Observations of the electron density, electron temperature, ion temperature, and ion drift line of sight velocity in the ionosphere from this incoherent scatter radar (ISR) are used in this study.

The Super Dual Auroral Radar Network (SuperDARN) is a network of high latitude coherent scatter radars (Greenwald et al., 1995; Chisham et al., 2007; Nishitani et al., 2019) that observe

149 line-of-sight plasma velocities in the F-region. These measurements are assimilated using the
150 map potential technique (Ruohoniemi and Baker, 1998), which uses an ionospheric
151 convection model to map the electrostatic potential pattern. Electrostatic equipotential lines
152 are streamlines of ionospheric convection flows. As the plasma drift velocity is perpendicular
153 to both the electric and magnetic fields in the F-region ($\vec{E} \times \vec{B}$ drift) the plasma convection
154 pattern can be directly inferred from the electric potential maps.

155 GNSS signals detected by NovAtel GPStation-6 receivers at the Kjell Henriksen Observatory
156 (KHO) (78.2° N, 16.0° E; 15.2° MLAT, 112.9° MLON) can be used to infer the effects of the
157 ionosphere on radio waves traveling through this medium. Amplitude scintillation is measured
158 using the S_4 index, which is the square root of the variance of received power divided by the
159 mean value of the received power (Briggs and Parkin, 1963). Phase scintillation is measured
160 using the σ_ϕ index, which is the standard deviation of the detrended carrier phase ϕ in radians
161 (Fremouw et al., 1978) over 60 seconds.

162 The IMF was observed by the Advanced Composition Explorer (ACE), which is a NASA
163 spacecraft orbiting the L1 Lagrangian point of the Earth-Sun system, roughly 1.54 million km
164 from the Earth (Zwickl et al., 1998). In addition to the x-, y- and z- components of the IMF the
165 clock angle, given by $\arctan \frac{|B_y|}{|B_z|}$, is also considered. When the clock angle is greater than 45
166 degrees either $|B_y| > |B_z|$ or $B_z < 0$, in either case a two-cell convection pattern is expected with
167 antisunward flow drawing plasma from day to night across the polar cap (Thomas and
168 Shepherd, 2018).

169 Total Electron Content (TEC) maps are used to put these measurements into context. These
170 were obtained from the Madrigal Database at the MIT Haystack Observatory (Ridout and
171 Coster, 2006; Vierinen et al., 2015). Two other indices are used within this study. The K_p index
172 is used as a proxy for disturbances to the geomagnetic field. The F10.7 cm solar flux is used as
173 a proxy for solar activity. These indices were both obtained from the UK Solar System Data
174 Centre (UKSSDC) at Rutherford Appleton Laboratory, UK.

175 **Results**

176 **Case study: 17th December 2014**

177 The 3-hourly K_p values observed on 17th December 2014 between 12:00 and 23:59 UT ranged
178 between 1- and 1+, indicating quiet conditions. The F10.7 cm solar flux was relatively high,
179 the value of 198.5 sfu is typical of solar maximum. The IMF observed by the ACE spacecraft
180 between 12:00 and 23:59 UT (Fig. 1) was characterised by a positive value for the IMF B_y (mean
181 value 3.9 nT). IMF B_z was more variable, but generally took smaller values (mean value of 1.7
182 nT). The clock angle was generally greater than 45° from 14 UT until 19 UT, and the
183 corresponding SuperDARN plots [\(discussed later in this section\)](#) show that a two cell
184 convection pattern dominated until at least 20 UT.

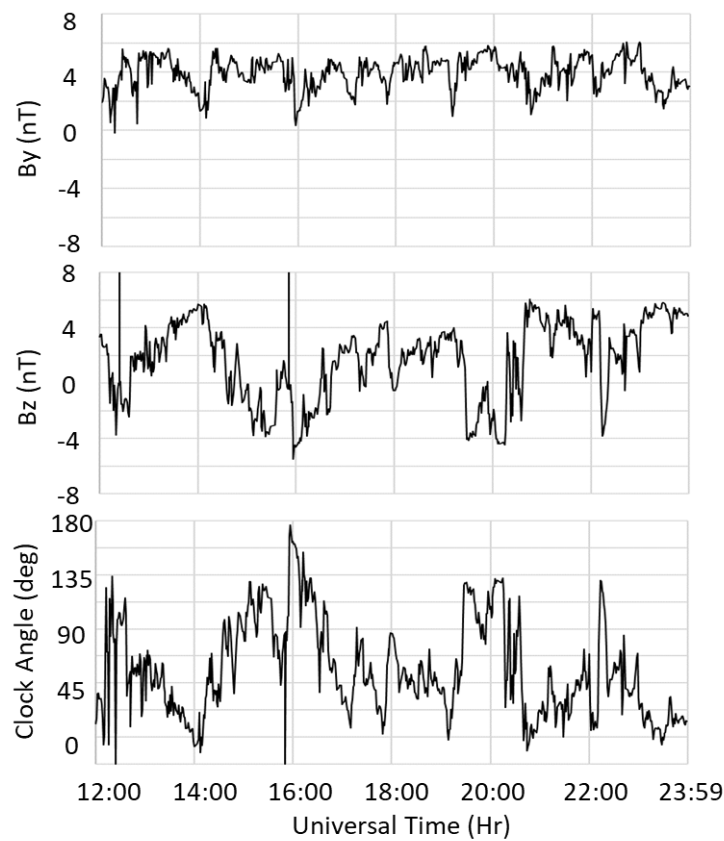


Fig. 1. The y- and z-components of the IMF, and the clock angle observed by the ACE spacecraft between 12:00 UT and 23:59 UT on 17th December 2014. The data have been time shifted to the nose of the Earth's bow shock.

Total Electron Content (TEC) maps (Fig. 2) show the overall plasma density throughout the high-latitude regions. The TEC maps at 12 UT and 15 UT show values of ~ 2 TECu (dark blue colour) in the polar cap. At 18 UT and 21 UT larger electron densities can be observed crossing the polar cap in a two cell convection pattern, with values of ~ 15 TECu (yellow colour), indicating that plasma produced by photoionisation on the dayside is being drawn into the polar cap. This plasma is being drawn into the polar cap during relatively quiet conditions ($K_p \sim 1$) and is consistent with a two cell convection pattern.

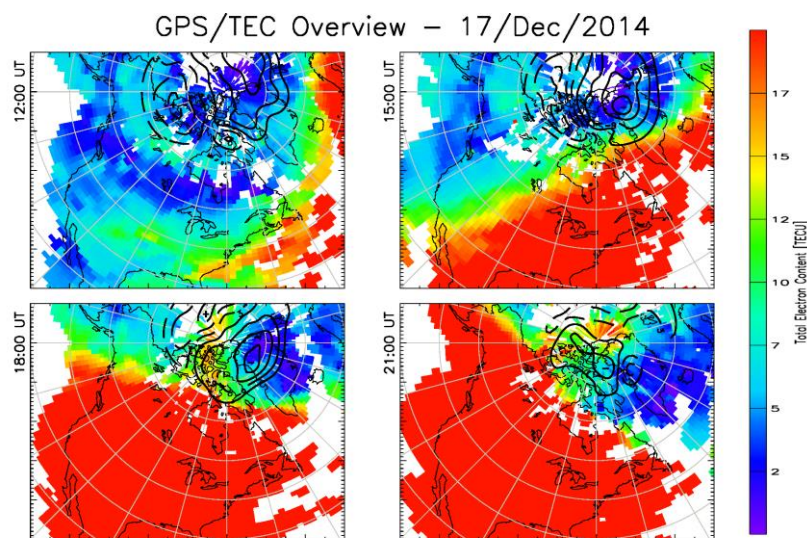
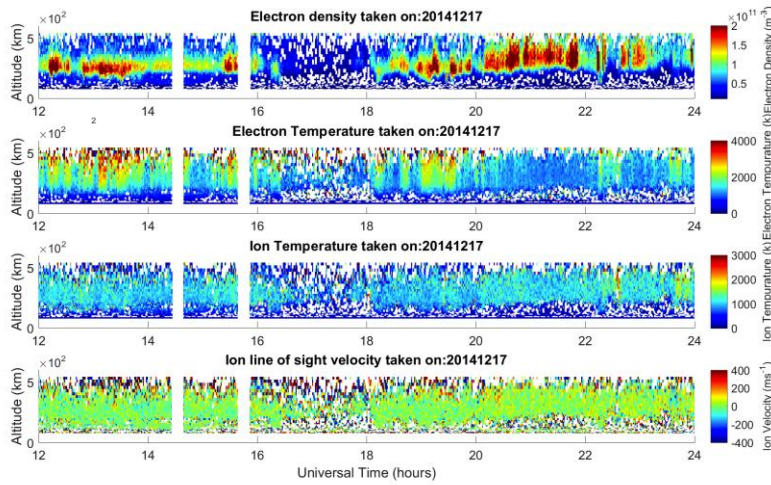


Fig. 2. TEC maps for the 17th December 2014 extrapolated from TEC collected by a network of GNSS receivers at three hourly intervals between 12 UT and 21 UT.

The electron densities and temperatures observed by the field-aligned 42 m dish of the EISCAT Svalbard Radar (ESR) between 12:00 UT and 23:59 UT are shown in Fig. 3. The scales on this plot have been chosen to enable a clear comparison with other figures presented in this paper. A clear depletion in the electron densities is observed between approximately 16 and 18 UT at all altitudes. The electron and ion temperatures are not elevated at this time with

204 values of approximately 1000 K, suggesting that this depletion is void of particle precipitation
 205 and did not arise from enhanced recombination due to Joule heating. The ESR does not
 206 show a substantial plasma velocity aligned with the radar beam. This radar observed at an
 207 elevation of 81.6° which is aligned with the magnetic field line in the F-region.
 208 There was no substantial component of velocity observed along the magnetic field line. In
 209 order to further investigate the electron density depletion, a line plot of the maximum
 210 detected electron density from 90-400 km is shown (Fig. 4). In addition to the maximum
 211 density two other values are present on the plot, the average value for the whole day, and
 212 35% of the average value. The depletion was defined as when the electron density dropped
 213 below the 35% line and, in this case, the depletion was defined as starting at 16:29 UT and
 214 ending at 18:00 UT.

215



216

217 **Fig. 3. Electron densities, electron temperatures, ion temperatures, and ion drift line of sight**
 218 **velocity measured by the 42 m dish of the ESR observing at an azimuth of 184.5° and an**
 219 **elevation of 81.6° between 12:00 UT and 23:59 UT on 17th December 2014.**

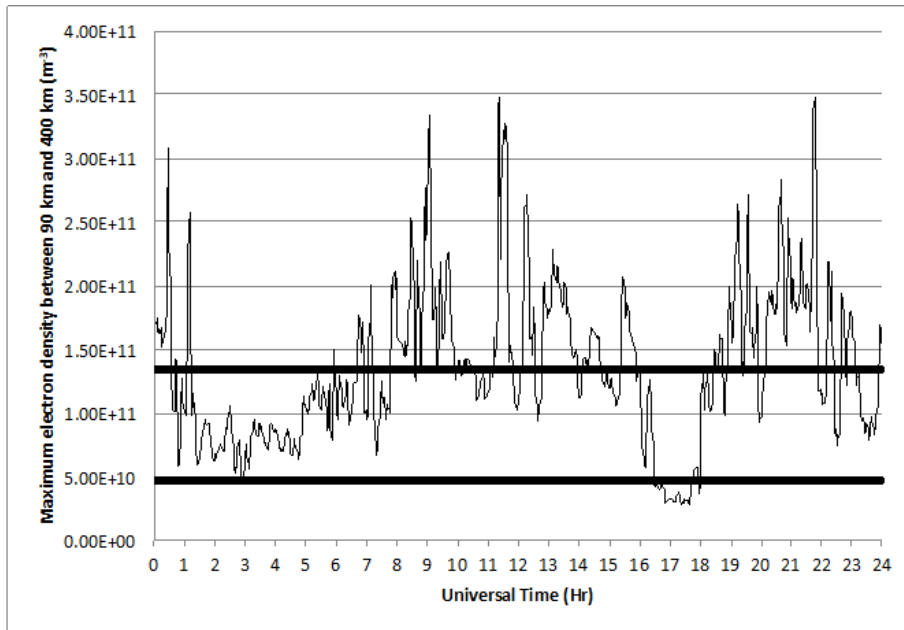
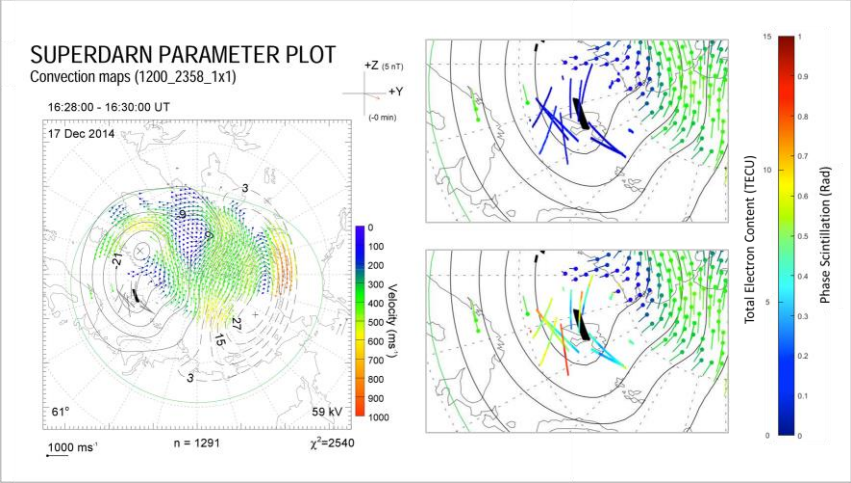


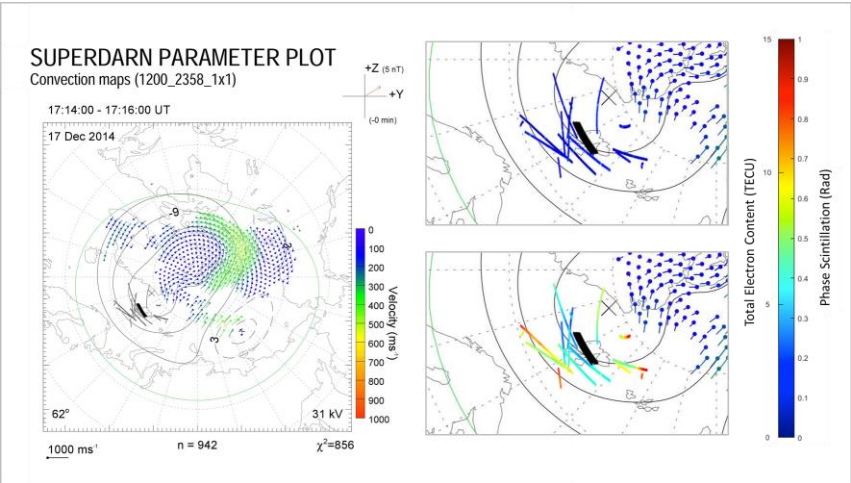
Fig. 4. Maximum electron density between 90 and 400 km for ESR 42 m observation on the 17th December 2014 at one minute resolution. A five point running mean was applied to these data. The upper horizontal line is the average value and the lower horizontal line is 35% of the average. A hole can be seen between 16:29 and 18:00 UT.

Fig. 5 shows the high-latitude convection pattern inferred from the SuperDARN radars for three representative times during the time that the electron density depletion was observed by the ESR. These clearly show a two cell convection pattern, with plasma drawn antisunward across the polar cap. The ESR observes at a given location, which rotates under the convection pattern. The depletion identified in Fig. 4 is indicated by a black line. At midwinter Svalbard is in perpetual darkness. On 14th December the ground level terminator is at a maximum latitude of 68° N, which corresponds to a maximum magnetic latitude of 76° MLAT at 21 UT. This depletion is nightward of the terminator and the SuperDARN convection patterns suggest that this plasma is circulating in perpetual darkness. It is interpreted as a polar hole.

236



237



238

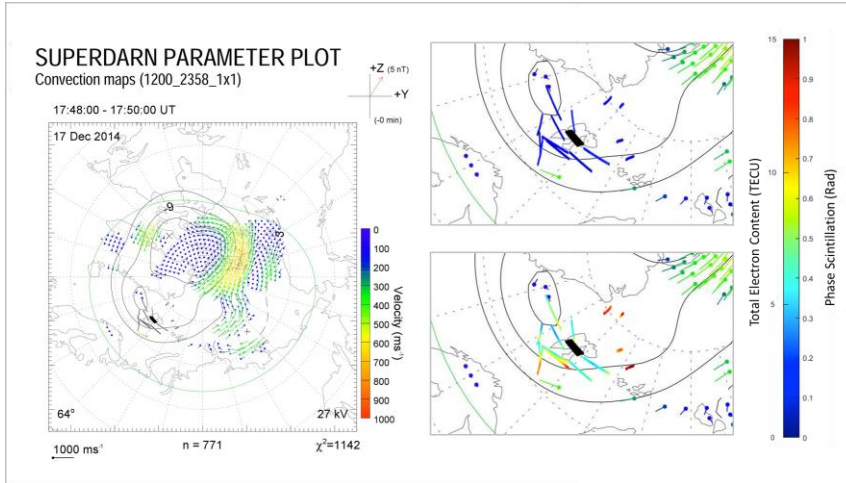


Fig. 5. Electric potential patterns inferred from the SuperDARN radars for 16:28 UT, 17:14 UT, and 17:48 UT on 17th December 2014 as a function of geomagnetic latitude and magnetic local time. Magnetic noon is at the top of each plot with dusk and dawn on the left- and right- hand sides respectively. Magnetic latitude is indicated by the grey dashed circular lines in 10.0° increments. The grey lines show the location of satellite passes from GNSS satellites, assuming an ionospheric intersection of 350 km. The SuperDARN plot from 16:28 UT includes satellite passes from 16:00-16:58 UT, the 17:14 UT plot includes satellite passes from 16:58-17:28 UT, and the 17:48 UT plot includes satellite passes from 17:28-18:02 UT. These time intervals were chosen as inspection of the whole SuperDARN data set at two minute resolution indicated that the convection patterns were relatively stable during these intervals. The right hand side of the panels show the area around the satellite passes in more detail. The multi-coloured colours represent phase scintillation (upper panel in each pair) and TEC (lower panel in each pair). The thick black line indicates the position of the polar hole observed with the 42 m dish of the EISCAT Svalbard Radar.

The data collected by the GNSS receiver was from the GPS, Galileo and GLONASS systems and the receiver provides the azimuth and elevation of the satellite with respect to the receiver. This was converted into a latitude and longitude using the radio wave path and assuming that the data corresponds to 350 km in altitude, in line with previous studies (e.g. Cervera and Thomas, 2006; Forte and Radicella, 2002). At low elevation angles the GNSS TEC and scintillation data can become unreliable due to multi-path issues, so observations at an

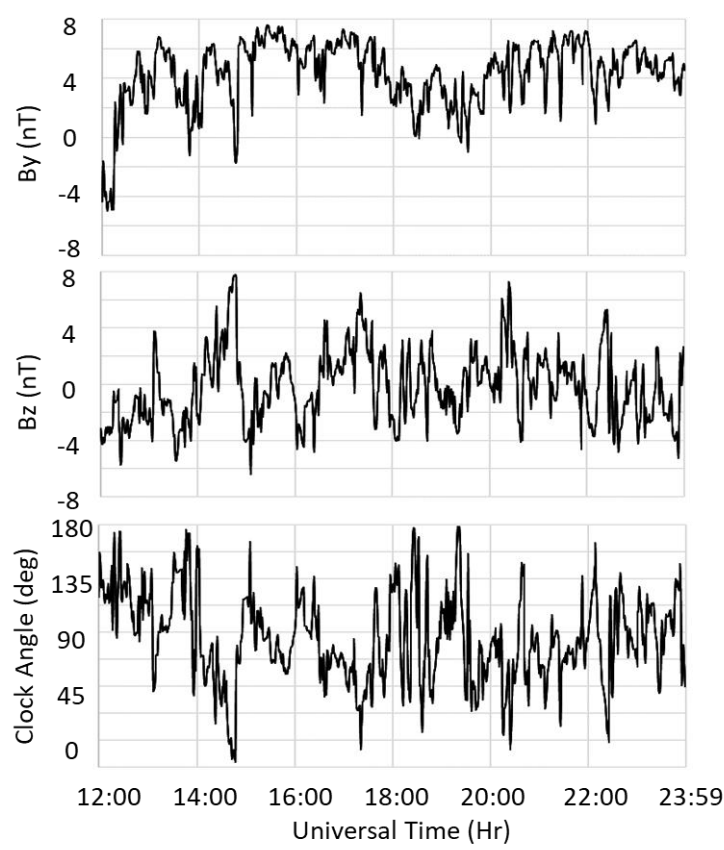
260 elevation of less than 30° were discarded. This cut of has been used in previous studies, for
261 example Mitchell et al. (2005). Signal lock times below 240 seconds were also discarded, in
262 line with previous studies (e.g. van der Meeren et al., 2015). The satellite tracks were overlaid
263 onto SuperDARN plots. (Fig. 5)

264 TEC and phase scintillation data from GNSS [receivers](#) were taken during
265 times when the polar hole was observed. This hole is observed for 1.5 hours and several
266 satellite paths are present during this time window. The GNSS TEC data clearly show lower
267 TEC levels at and around the area marked by the ESR as a hole and, on some of the satellite
268 trajectories, sharp changes can be seen with the edge of the hole. A one-to-one
269 correspondence between the GNSS TEC data and the EISCAT data is neither expected or
270 observed. It is highly likely that the polar hole will evolve during the time for which it is
271 observed, and therefore the plots in figure 5 include both spatial and temporal variation. The
272 ESR observes the polar hole for 91 minutes and the plasma velocity inferred from [the electric](#)
273 [potential patterns inferred from the SuperDARN radars](#) (figure 5) at this location is of the order
274 of 150 ms^{-1} , indicating that the polar hole has a horizontal extent of some 800 km in a
275 direction parallel to the plasma flow.
276 [aligned with the magnetic field, suggesting that the plasma flow is primarily in the horizontal](#)
277 In summary the combination of the EISCAT and GNSS TEC measurements indicate
278 that the polar hole is present for an extended period of time (of the order of hours) over a
279 large (hundreds of km) spatial scale.

280 Panels showing the location of phase scintillation on the satellite tracks are also shown in
281 figure 5. A threshold of 0.2 rad was used to identify phase scintillation. [Different authors](#)
282 [have used different thresholds for phase scintillation, including 0.2 rad \(e.g. van der Meeren,](#)
283 [2015\), 0.25 rad \(e.g. Alfonsi et al., 2011\) and 0.3 rad \(e.g. Kinrade et al., 2013\).](#) The purpose of
284 [using a](#) low threshold [within the present study](#) was to ensure that any possible indication
285 of phase scintillation was included. Since TEC and scintillation are collected simultaneously,
286 comparing the two might be expected to show increased scintillation where there are changes
287 in TEC. No scintillation was been seen on the edges of the holes.

288 **Case study 2: 10th December 2015**

289 The F10.7cm solar flux for this case was lower than in the first study, with a value of 108.5 sfu.
290 The K_p index was higher, with values of 3 from 12 to 18 UT and values of 4 at 21 and 24 UT,
291 indicating an active state, but not storm levels. Once again the IMF was variable, with B_z taking
292 positive and negative values. B_y was consistently larger than B_z and dominated. As in the
293 previous case study a two cell convection pattern was observed.

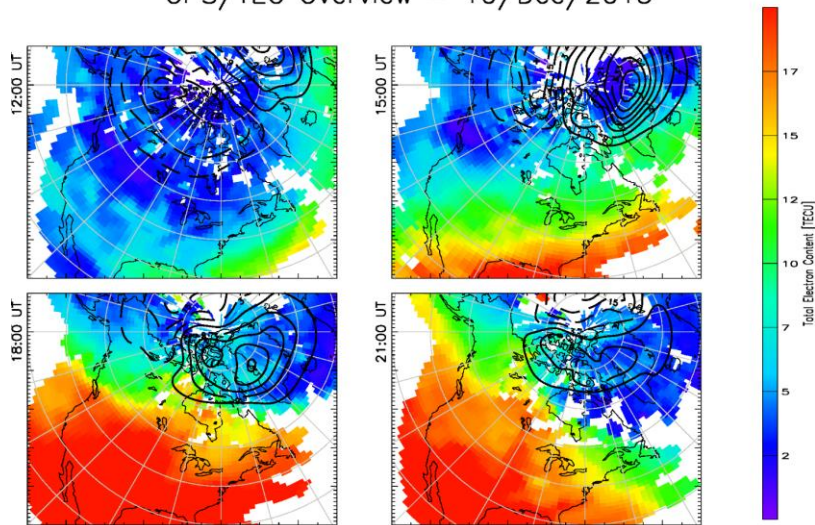


294
295 **Fig. 6. The y- and z-components of the IMF, and the clock angle observed by the ACE**
296 **spacecraft between 12:00 and 23:59 UT on 10th December 2015, in the same format as Fig.**
297 **1. The data have been time shifted to the nose of the Earth's bow shock.**

298

299 The TEC maps at 18 and 21 UT are shown in Fig. 7. As in the previous case study these indicate
300 higher density plasma produced at lower latitudes being drawn across the polar cap within
301 the high latitude convection pattern, with this effect maximising at 21 UT.

GPS/TEC Overview – 10/Dec/2015



302

303 **Fig. 7. TEC maps for the 10th December 2015 extrapolated from TEC collected by a network**
304 **of GNSS receivers at three hourly intervals between 12 and 21 UT.**

305 The 42 m ESR observations (Fig. 8) for this day show an electron density depletion that
306 contains all the previously discussed markers, with no significant velocity in the field aligned
307 direction.

308 Using the same method as in the previous case the hole was identified with the start and end
309 times given as 15:15 and 16:43 UT. The 32 m ESR observations (Fig. 15) show a depletion at
310 around 15 UT.

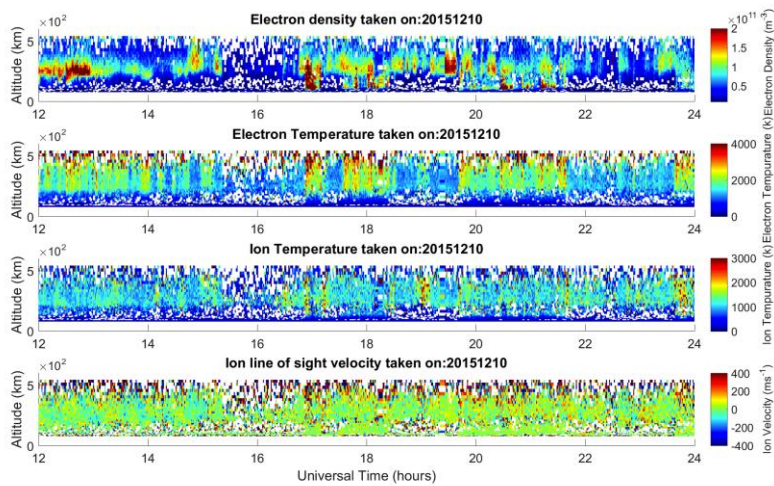
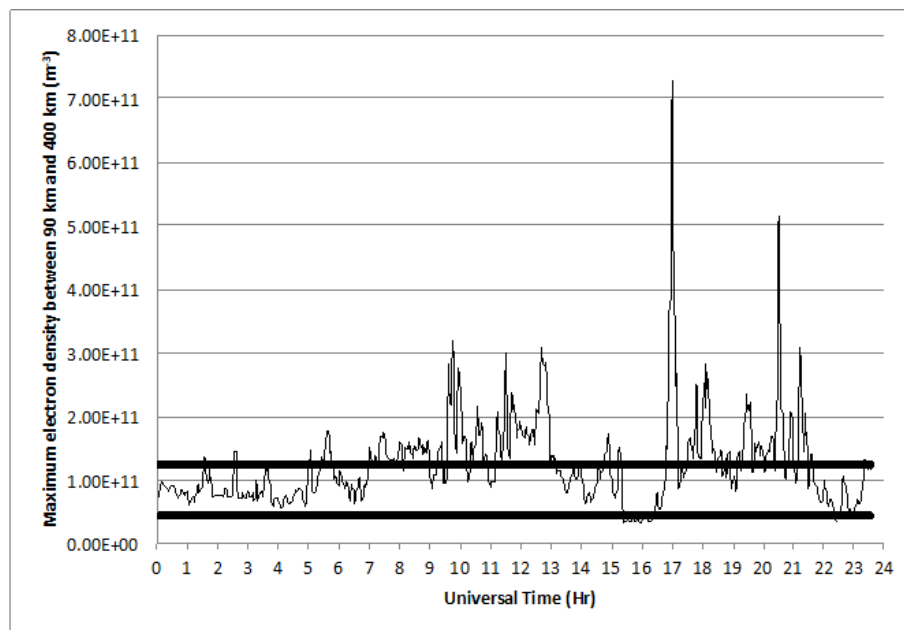
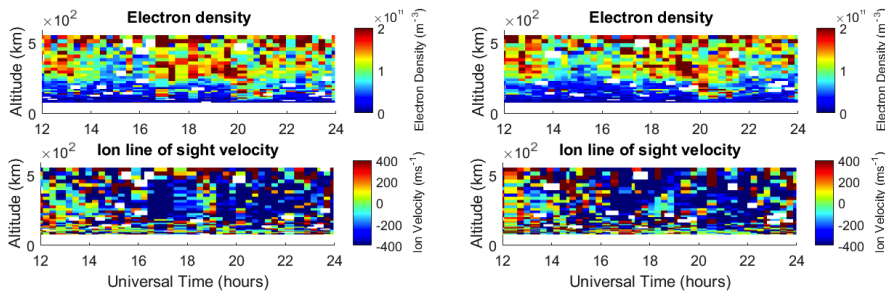


Fig. 8. Electron densities, electron temperatures, ion temperatures, and ion drift line of sight velocity measured by the 42 m dish of the ESR observing at an azimuth of 184.5° and an elevation of 81.6° between 12:00 and 23:59 UT on 10th December 2015.



316 Fig. 9. As Fig. 4 but for 10th December 2015. A polar hole can be seen between 15:24 and
 317 16:25 UT.



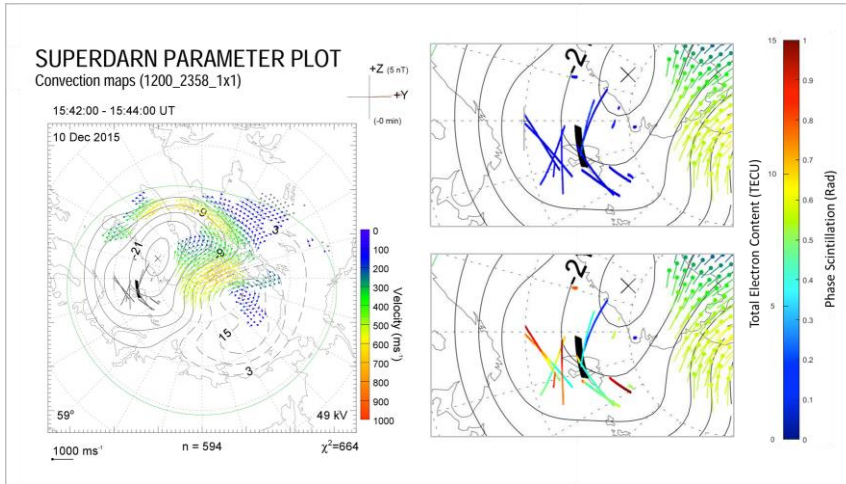
318
 319 Fig. 10. Electron densities and ion drift line of sight velocities observed by the 32 m dish of
 320 the ESR at -43° azimuth and 30° elevation (left hand side) and at -14° azimuth and 30°
 321 elevation (right hand side) between 12:00 and 23:59 UT on 10th December 2015.

322 The high-latitude convection pattern was inferred from the SuperDARN radars (Fig. 11), with
 323 the location of the polar hole observed in the 42 m ESR observations, and GNSS TEC and phase
 324 scintillation measurements overlaid as in the previous case study. The 32 m ESR observations
 325 (Fig. 9) were directed poleward; indicating that this a polar hole rather than the ionospheric
 326 trough, which would be located equatorward of the radar. A substantial plasma velocity of
 327 some 300 ms⁻¹ towards the radar was observed at 16:00 UT, indicating cross-polar flow in
 328 the equatorward direction. The high-latitude convection pattern inferred from the
 329 SuperDARN radars also shows antisunward cross-polar flow, but with
 330 a more asymmetric convection pattern than was observed on 17th December 2014. On 10th
 331 December 2015 there was a clear dominant dusk cell, drawing plasma across the polar cap
 332 from the pre-noon sector. The polar hole observed with the 42 m dish of the ESR was in the
 333 sunward return flow in the dusk convection cell.

334 The phase scintillation plot for 15:16 to 16:14 UT (upper right panel of Fig. 11) has some
 335 satellite trajectories passing through the hole boundary, but displays no significant
 336 scintillation on any of the paths. The later plot (second panel from the bottom on the right
 337 panel of Fig. 11) does contain phase scintillation seen however none of the elevated
 338 scintillation matches up to hole boundaries, instead, the scintillation is seen in regions of high
 339 and elevated electron density.

340

341



348

349 Discussion

350 A series of polar ionospheric holes have been detected in the high latitude nightside
351 ionosphere in case studies close to winter solstice, under varying solar intensities and
352 geomagnetic disturbance levels. The first study on 17th December 2014 saw high levels of solar
353 activity (198.5 sfu) and quiet geomagnetic conditions. The second case study, on 10th
354 December 2015 also had lower levels of solar activity of (108.5 sfu), but had more active
355 geomagnetic conditions ($K_p=3$) than in the previous study. A third case study, under quiet
356 geophysical conditions ($K_p \leq 2$) and moderate solar activity (F10.7 cm solar flux = 116.7 sfu) on
357 12th December 2015 showed similar results (not shown).

358 Ionospheric polar holes contain much lower electron densities than those detected through
359 the rest of the day, this study used the maximum density at a given time dropping 35% below
360 the daily average maximum density to identify these holes. The changes in electron density
361 are associated with large electron density gradients. Table 1 shows the electron density
362 gradients and average hole electron density, based on observations from the ESR 42 m. The
363 average polar hole density observed in this study is comparable to those previously reported
364 of 10^8 - 10^{11} electrons·m⁻³ (Obara and Oya, 1989, Benson and Grebowsky, 2001). Steep electron
365 density gradients are observed at the edges of the holes, these are expressed in units of
366 $\Delta N_e \cdot m^{-3} \cdot h^{-1}$. Although these gradients are expressed in units of h⁻¹ they were calculated from
367 successive observations by the ESR 42 m (these measurements are typically one minute
368 apart). The spatial extent of these holes was at least several hundred kilometres, as inferred
369 from the GNSS TEC measurements (all studies) and the ESR 32 m observations (case study
370 from 17th December 2014). Polar holes are usually associated with quiet geomagnetic
371 conditions ($K_p < 2$). It is notable that, on 10th December 2015, a polar hole was observed under
372 more active geomagnetic conditions ($K_p=3$).

Date	1 st Edge $\Delta N_e \cdot m^{-3} \cdot h^{-1}$	2 nd Edge $\Delta N_e \cdot m^{-3} \cdot h^{-1}$	Average Hole $N_e \cdot m^{-3}$
17/12/2014	1.0E+11	9.1E+10	4.0E+10
10/12/2015	3.5E+11	1.6E+11	2.2E+10
12/12/2015	7.9E+10	1.0E+11	1.8E+10

Table 1 – The electron density gradient at each edge of the polar hole and the average electron density inside the hole at 350 km observed by ESR 42 m.

373

374 The IMF conditions during the time when the polar holes were observed, and for several hours
375 beforehand, were appropriate for antisunward cross-polar convection. The ground level solar
376 terminator for winter is only above 70° MLAT between 15 UT and slightly after 21 UT, reaching
377 a maximum latitude of just under 76° MLAT on the dayside at around 21 UT, creating the
378 possibility that plasma within the high-latitude convection pattern could circulate in perpetual
379 darkness, thus undergoing recombination whilst simultaneously being insulated from
380 photoionisation, or precipitation, creating a polar hole.

381 Phase scintillation has previously been observed to coincide with large plasma gradients such
382 as on the edge of ionospheric enhancements such as polar cap patches (Jin et al., 2017), the
383 tongue of ionisation (van der Meeren et al., 2014), plasma structures associated with the
384 aurora (Kinrade et al., 2013; Oksavik et al., 2015; van der Meeren et al., 2015) and the mid-
385 latitude trough (Pryse et al., 1991). The structures that cause scintillation arise due to the
386 Gradient Drift Instability and/or the Kelvin Helmholtz Instability (Keskinen and Ossakow, 1983;
387 Carlson et al., 2008). In the present study, once the boundaries and the large electron density
388 gradients associated with them were identified these boundaries were investigated for
389 elevated levels of phase scintillation. A threshold of 0.2 rad was used, the purpose of this low
390 value was to ensure that any possible indication of phase scintillation was included. Across all
391 of the observed GNSS points coinciding with the polar hole boundaries no such levels of phase
392 scintillation were detected. Phase scintillation usually dominates at high latitude (e.g., Prikryl
393 et al., 2015), although amplitude scintillation has also been observed (e.g. Mitchell et al.,
394 2005). The present study focuses upon phase scintillation as no amplitude scintillation,
395 defined as when the S4 index was greater than 0.2, was observed on any of the TEC gradients
396 at the boundaries of the polar holes.

397 This is not the first time a plasma density enhancement has been observed without
398 corresponding phase scintillation. Van der Meeren et al. (2016) observed a Sun-aligned polar
399 cap arc under quiet geomagnetic conditions without corresponding scintillation. In the
400 present study some phase scintillation was observed, however, these points coincide with
401 increases in TEC and the edges of spikes in electron densities at other locations. In the second
402 case study (10th December 2015) phase scintillation was observed at a point associated with
403 elevated TEC (lower right panels of Fig. 11), but this was not associated with the assumed
404 boundary of the polar hole.

405 When phase scintillation was observed it was always associated with electron density
406 gradients, but converse is not always true. Therefore it appears that some minimum level of
407 overall electron density is needed for phase scintillation to occur. Given that it is the presence
408 of small scale structures that cause scintillation, this suggests that these small scale structures
409 have not arisen.

410 Figure 12 shows phase scintillation as a function of TEC and TEC rate of change. This figure
411 also includes data from a third study, using data from 12th December 2015, which was
412 consistent with the interpretation presented here, but which has been omitted in the interest
413 of concision. Low scintillation can be seen at all TEC levels and for a majority of the range of
414 TEC rates of change. On the other hand, elevated scintillation levels are only seen above
415 approximately 6 TECU suggesting that a minimum electron density is required. This is not a
416 new idea, in his review paper Aarons (1982) commented 'if the ionosphere is perturbed on a
417 percentage basis, *change in N* in the trough will be small since *N* is low; scintillations will then
418 be low.' The current paper provides observational evidence to support this suggestion that a
419 minimum electron density is required. The current paper is also consistent with suggestions
420 made by Prikryl et al. (2015), where the strongest phase scintillations were found to be highly
421 collocated with regions that are ionospheric signatures of the coupling between the solar
422 wind and magnetosphere. Polar holes appear to be areas of weak coupling, hence less
423 scintillation.

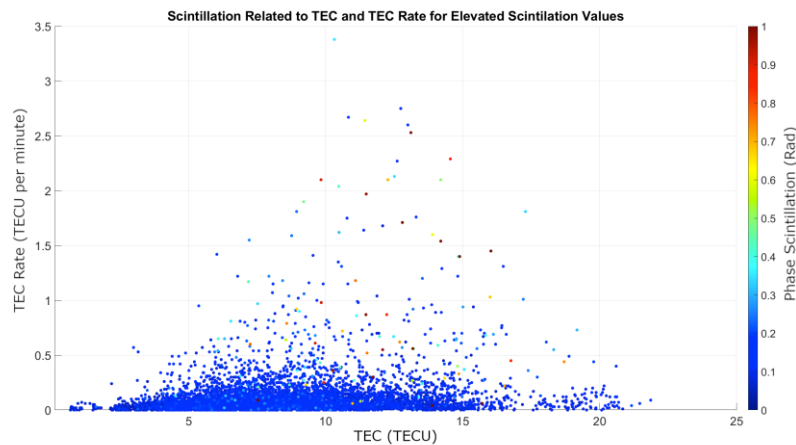


Fig. 12 – Phase scintillation as a function of TEC and the TEC rate of change per minute for 17th December 2014, 12th December 2015 and 10th December 2015.

In this study the phase scintillation index (σ_ϕ) has been calculated across a 60 second interval, in line with common practice within this field. However, if this index was computed across a shorter time interval, then it is possible that elevated values of σ_ϕ may be associated with the edge of the polar hole. This would be an interesting topic for a future paper. Further developments upon this work would expand the observations of the polar holes discussed to a larger number of examples under a wider range of geophysical conditions. Polar ionospheric holes could be tracked by making observations with a higher temporal resolution at a large number of regularly spaced locations. The advent of EISCAT-3D (McCrea et al., 2015), which will give unprecedented temporal and spatial coverage, will enable such studies in the European sector of the high-latitude ionosphere. The ability to observe the evolution of polar holes over time will give a new, deeper, understanding of these features and how they influence practical radio systems such as GNSS.

Conclusions

Polar ionospheric holes are regions of electron density depletions containing large electron density gradients at their boundaries. These holes were observed during geomagnetically quiet and moderately disturbed conditions and under a range of solar activities using the

444 EISCAT Svalbard Radar (ESR) and measurements from GNSS [receivers](#). Steep
445 electron density gradients have been associated with phase scintillation at GNSS frequencies
446 in previous studies, however no enhanced scintillation was detected upon the electron
447 density gradients at these boundaries. Phase scintillation was only observed when electron
448 density levels were elevated above 6 TECU and a gradient was present implying that both a
449 minimum electron density level and a sharp gradient in the electron density must be present
450 for instability mechanisms to produce scintillation structures.

451 **Author contribution**

452 This work was led by Luke Jenner, under the guidance of Alan Wood. Kjellmar Oksavik provided
453 the GNSS TEC and scintillation data, together with guidance regarding their interpretation. Tim
454 Yeoman and Alexandra Fogg provided the SuperDARN electric potential maps, together with
455 guidance regarding their interpretation. Anthea Coster provided the TEC maps, together with
456 guidance regarding their interpretation. All authors contributed to the discussion. The
457 manuscript was prepared by Luke Jenner and Alan Wood.

458 **Competing interests**

459 The authors declare that they have no conflict of interest.

460 **Acknowledgements**

461 EISCAT is an international facility supported by the national science councils of China, Finland,
462 Japan, Norway, Sweden, and the United Kingdom. The assistance of Ingemar Häggström and
463 colleagues at the EISCAT Scientific Association in running the experiments is gratefully
464 acknowledged. The data used in this paper is publicly available at <https://www.eiscat.se>. The
465 assistance of Steve Crothers and Matthew Wild at Rutherford Appleton Laboratory with the
466 data processing is gratefully acknowledged. The GNSS TEC and scintillation data were provided
467 by Kjellmar Oksavik at the University of Bergen, and is supported by the Norwegian Research
468 Council under contracts 212014 and 223252. The authors acknowledge the use of SuperDARN
469 data, data for which is available at <https://vt.superdarn.org>. SuperDARN is a collection of
470 radars funded by national scientific funding agencies of Australia, Canada, China, France, Italy,

471 Japan, Norway, South Africa, United Kingdom and the United States of America.’ Alexandra
472 Fogg is supported by a studentship from the Science and Technology Facilities Council (UK).
473 The assistance of Nathan Brown with the production of Fig. 5 and Fig. 11 is gratefully
474 acknowledged. GPS TEC data products and access through the Madrigal distributed data
475 system are provided to the community (<http://www.openmadrigal.org>) by the Massachusetts
476 Institute of Technology (MIT) under support from US National Science Foundation grant AGS-
477 1242204. Data for TEC processing is provided from the following organizations: UNAVCO,
478 Scripps Orbit and Permanent Array Center, Institut Geographique National, France,
479 International GNSS Service, The Crustal Dynamics Data Information System (CDDIS), National
480 Geodetic Survey, Instituto Brasileiro de Geografia e Estatística, RAMSAC CORS of Instituto
481 Geográfico Nacional de la República Argentina, Arecibo Observatory, Low-Latitude
482 Ionospheric Sensor Network (LISN), Topcon Positioning Systems, Inc., Canadian High Arctic
483 Ionospheric Network, Centro di Ricerche Sismologiche, Système d’Observation du Niveau des
484 Eaux Littorales (SONEL), RENAG : REseau NATional GPS permanent, GeoNet - the official source
485 of geological hazard information for New Zealand, GNSS Reference Networks, Finnish
486 Meteorological Institute, and SWEPOS - Sweden. Access to these data is provided by madrigal
487 network via: <http://cedar.openmadrigal.org/>. The K_p index and F10.7 cm solar flux were
488 obtained from the UK Solar System Data Centre at Rutherford Appleton Laboratory. These can
489 be accessed at <https://www.ukssdc.ac.uk/>. The IMF data were provided by N. Ness and
490 obtained from the CDAWeb at <https://cdaweb.gsfc.nasa.gov/>.

491

References

- Aarons, J.: Global Morphology of Ionospheric Scintillations, *Proceedings of the IEEE*, 70, 4, 360-378, doi: 10.1109/PROC.1982.12314, 1982.
- Alfonsi, L., Spogli, L., De Franceschi, G., Romano, V., Aquino, M., Dodson, A., and Mitchell C. N.: Bipolar climatology of GPS ionospheric scintillation at solar minimum, *Radio Sci.*, 46, RS0D05, doi:10.1029/2010RS004571, 2011.
- Anderson, D. N., Buchau, J., and Heelis R. A.: Origin of density enhancements in the winter polar cap ionosphere, *Radio Sci.*, 23, 513-519, doi: 10.1029/RS023i004p00513, 1988.
- Benson, R., and Grebowsky, J.: Extremely low ionospheric peak altitudes In the polar hole region, *Radio Sci.*, 36, 277-285, doi:10.1029/1999rs002401, 2001.
- Briggs, B.H., and Parkin I. A.: On the variation of radio star and satellite scintillation with zenith angle, *J. Amos. Terr. Phys.*, 25, 339-365, doi:10.1016/0021-9169(63)90150-8, 1963.
- Brinton, H., Grebowsky, J., and Brace L.: The high-latitude winter F-region at 300 km: Thermal plasma observations from Ae-C, *J. Geophys. Res.*, 83, 4767-4776, doi:10.1029/Ja083ia10p04767, [https://doi.org/10.1016/0273-1177\(91\)90317-D](https://doi.org/10.1016/0273-1177(91)90317-D), 1978.
- Buchau, J. and Reinisch, B. W.: Electron density structures in the polar F region, *Adv. Space Res.*, 11(10), 29-37, 1991.
- Buchau, J., Reinisch, B. W., Weber, E. J., and Moore, J. G.: Structure and dynamics of the winter polar cap F region, *Radio Sci.*, 18, 995-1010, <https://doi.org/10.1029/RS018i006p00995>, 1983.
- Carlson, H. C., Oksavik, K., Moen, J., van Eyken, A.P., and Guio, P.: ESR mapping of polar-cap patches in the dark cusp, *Geophys. Res. Lett.*, 29 (10), 1386, doi:10.1029/2001GL014087, 2002.
- Carlson, H. C., Oksavik, K., Moen, J., and Pedersen, T.: Ionospheric patch formation: Direct measurements of the origin of a polar cap patch, *Geophys. Res. Lett.*, 31, L08806, doi:10.1029/2003GL018166, 2004.

518 Carlson, H. C., Moen, J., Oksavik, K., Nielsen, C. P., McCrea, I. W., Pedersen, T. R., and Gallop,
519 P.: Direct observations of injection events of subauroral plasma into the polar cap, *Geophys.*
520 *Res. Lett.*, 33, L05103, doi:10.1029/2005GL025230, 2006.

521 Carlson, H., Oksavik, K., and Moen, J.: On a new process for cusp irregularity production,
522 *Ann. Geophys.*, 26, 2871-2885, doi:10.5194/angeo-26-2871-2008, 2008.

523 Cervera, M., and Thomas, R.: Latitudinal and temporal variation of equatorial ionospheric
524 irregularities determined from GPS scintillation observations, *Ann. Geophys.*, 24, 3329-3341,
525 doi:10.5194/Angeo-24-3329-2006, doi: 10.5194/angeo-24-3329-2006, 2006.

526 Chisham, G., Lester, M., Milan, S. E., Freeman, M. P., Bristow, W. A., Grocott, A., McWilliams,
527 K. A., Ruohoniemi, J. M., Yeoman, T. K., Dyson, P. L., Greenwald, R. A., Kikuchi, T., Pinnock, M.,
528 Rash, J. P. S., Sato, N., Sofko, G. J., Villain, J.-P., and Walker, A. D. M.: A decade of the Super
529 Dual Auroral Radar Network (SuperDARN): Scientific achievements, new techniques and
530 future directions, *Surv. Geophys.*, 28, 33–109, doi:10.1007/s10712-007-9017-8, 2007.

531 Cowley, S.W.H. and Lockwood, M.: Excitation and decay of solar-wind driven flows in the
532 magnetosphere-ionosphere system, *Ann. Geophys.*, 10, 103, 1992.

533 Crowley, G.: Critical Review of patches and blobs, in *Polar Cap Boundary Phenomena*, in: *URSI*
534 *Review of Radio Science 1993-1996*, edited by Stone, W. R., published for the International
535 Union of Radio Science, Oxford University Press, 619-648, doi:10.1029/2009JA014985, 1996.

536 [De Franceschi, G., Spogli, L., Alfonsi, L. et al. The ionospheric irregularities climatology over](#)
537 [Svalbard from solar cycle 23. *Sci Rep* 9, 9232 \(2019\) doi:10.1038/s41598-019-44829-5](#)

538 Elmas, Z., Forte, B. and Aquino, A.: The impact of ionospheric scintillation on the GNSS receiver
539 signal tracking performance and measurement accuracy, *URSI General Assembly and*
540 *Scientific Symposium*, doi 10.1109/URSIGASS.2011.6123719, 2011.

541 [Forte B. \(2005\), Optimum detrending of raw GPS data for scintillation measurements at](#)
542 [auroral latitudes, *Journal of Atmospheric and Solar-Terrestrial Physics*, Vol. 67, N. 12,](#)
543 [doi:10.1016/j.jastp.2005.01.011.](#)

544 Forte, B., and Radicella, S.: Problems in data treatment for ionospheric scintillation
545 measurements, *Radio Sci.*, 37, 81-85, doi:10.1029/2001rs002508, 2002.

546 Foster, J. C.: Ionospheric signatures of magnetospheric convection, *J. Geophys. Res.*, 89, 855-
547 865, 10.1029/JA089iA02p00855, 1984.

548 Fremouw, E. J., Leadabrand, R. L., Livingston, R. C., Cousins, M. D., Rino, C. L., Fair, B. C., and
549 Long, R. A.: Early results from the DNA wideband satellite experiment—Complex-signal
550 scintillation, *Radio Sci.*, 13, 167–187, doi:10.1029/RS013i001p00167, 1978.

551 Greenwald, R. A., Baker, K. B., Dudeney, J. R., Pinnock, M., Jones, T. B., Thomas, E. C., Vilain,
552 J. P., Cerisier, J. C., Senior, C., Hanuise, C., Hunsucker, R. D., Sofko, G., Koehler, J., Neilsen, E.,
553 Pellinen, R., Walker, A. D. M., Sato, N., and Yamagishi, H.: DARN/SuperDARN: A global view
554 of high latitude convection, *Space Sci. Rev.*, 71, 761-796. doi:10.1007/BF00751350, 1995.

555 Hapgood, M. (2017), Satellite navigation—Amazing technology but insidious risk: Why
556 everyone needs to understand space weather, *Space Weather*, 15, 545–548,
557 doi:10.1002/2017SW001638.

558 Jin, Y., Moen, J. I., Miloch, W. J., Clausen, L. B. N., and Oksavik, K.: Statistical study of the GNSS
559 phase scintillation associated with two types of auroral blobs, *J. Geophys. Res. Space Physics*,
560 121, doi:10.1002/2016JA022613, 2016.

561 Jin, Y., Moen, J., Oksavik, K., Spicher, A., Clausen, L., Miloch, W.: GPS scintillations associated
562 with cusp dynamics and polar cap patches. *J. Space Weather Space Clim.*, 7, A23
563 doi:10.1051/swsc/2014019, 2017.

564 Jones, D. G., Walker I. K., and Kersley, L.: Structure of the poleward wall of the trough and the
565 inclination of the geomagnetic field above the EISCAT radar, *Ann. Geophys.*, 15, 740-746,
566 <https://doi.org/10.1007/s00585-997-0740-8>, 1997.

567 Kersley, L., Russell, C. D., and Rice, D. L.: Phase scintillation and irregularities in the northern
568 polar ionosphere, *Radio Sci.*, 30, 619, doi:10.1029/94RS03175,1995.

569 Kersley, L., Jenkins, D. B., and Edwards, K. J.: *Nature Phys .Sci.*, 239, 11, 1972.

570 Keskinen, M. J. and Ossakow, S. L.: Theories of high-latitude ionospheric irregularities: A
571 review, *Radio Sci.*, 18, 1077-1091, doi:10.1029/RS018i006p01077, 1983.

572 Kinrade, J., Mitchell, C. N., Smith, N. D., Ebihara, Y., Weatherwax, A. T., and Bust, G. S.: GPS
573 phase scintillation associated with optical auroral emissions: First statistical results from the
574 geographic South Pole, *J. Geophys. Res. Space Physics*, 118, 2490–2502,
575 doi:10.1002/jgra.50214, 2013.

576 Lockwood, M., and Carlson, H. C.: Production of polar cap electron density patches by
577 transient magnetopause reconnection, *Geophys. Res. Lett.*, 19, 1731 – 1734, 1992.

578 [McCaffrey, A. M., & Jayachandran, P. T. \(2019\). Determination of the refractive contribution](#)
579 [to GPS phase “scintillation”. *Journal of Geophysical Research: Space Physics*, 124, 1454– 1469.](#)
580 <https://doi.org/10.1029/2018JA025759>

581 McCreia, I., Aikio, A., Alfonsi, L., Belova, E., Buchert, S., Clilverd, M., Engler, N., Gustavsson, B.,
582 Heinselman, C., Kero, J., Kosch, M., Lamy, H., Leyser, T., Ogawa, Y., Oksavik, K., Pellinen-
583 Wannberg, A., Pitout, F., Rapp, M., Stanislawska, I., and Vierinen, J.: The science case for the
584 EISCAT_3D radar, *Progress in Earth and Planetary Science*, 2:21, doi:10.1186/s40645-015-
585 0051-8, 2015.

586 Millward, G. H., Moffett, R. J., Balmforth, H. F., and Rodger, A. S.: Modeling the ionospheric
587 effects of ion and electron precipitation in the cusp, *J. Geophys. Res.*, 104, 24,603,
588 <https://doi.org/10.1029/1999JA900249>, 1999.

589 Mitchell, C. N., Alfonsi, L., De Franceschi, G., Lester, M., Romano, V., and Wernik, A. W.: GPS
590 TEC and scintillation measurements from the polar ionosphere during the October 2003
591 storm, *Geophys. Res. Lett.*, 32, L12S03, doi:10.1029/2004GL021644, 2005.

592 Nishimura, Y., Lyons, L. R., Zou, Y., Oksavik, K., Moen, J. I., Clausen, L. B., Donovan, E. F.,
593 Angelopoulos, V., Shiokawa, K., Ruohoniemi, J. M., Nishitani, N., McWilliams, K. A., and Lester,
594 M.: Day-night coupling by a localized flow channel visualized by polar cap patch propagation,
595 *Geophys. Res. Lett.*, 41, 3701-3709, doi:10.1002/2014GL060301, 2014.

596 Nishitani, N., Ruohoniemi, J. M., Lester, M., Baker, J. B. H., Koustov, A. V., Shepherd, S. G.,
597 Chisham, G., Hori, T., Thomas, E. G., Makarevich, R. A., Marchaudon, A., Ponomarenko, P.,
598 Wild, J. A., Milan, S. E., Bristow, W. A., Devlin, J., Miller, E., Greenwald, R. A., Ogawa, T.,
599 and Kikuchi, T.: Review of the accomplishments of mid-latitude Super Dual Auroral Radar
600 Network (SuperDARN) HF radars, *Prog. Earth Planet. Sci.*, 6, 27, doi:10.1186/s40645-019-
601 0270-5, 2019.

602 Obara, T., And Oya, h.: Observations of polar cusp and polar cap ionospheric irregularities and
603 formation of ionospheric holes using topside sounder onboard Exos-C (Ohzora) satellite,
604 *Journal of Geomagnetism and Geoelectricity*, 41, 1025-1042, doi:10.5636/Jgg.41.1025, 1989.

605 Oksavik, K., Barth, V. L., Moen, J., and Lester, M.: On the entry and transit of high-density
606 plasma across the polar cap, *J. Geophys. Res.*, 115, A12308, doi:10.1029/2010JA015817,
607 2010.

608 Oksavik, K., van der Meeren, C., Lorentzen, D. A., Baddeley, L. J., and Moen, J.: Scintillation
609 and loss of lock from poleward moving auroral forms in the cusp ionosphere, *J. Geophys. Res.*
610 *Space Physics*, 120, doi:10.1002/2015JA021528, 2015.

611 Parkinson, M. L., Dyson, P. L., Pinnock, M., Devlin, J. C., Hairston, M. R., Yizengaw, E., and
612 Wilkinson, P. J.: Signatures of the midnight open-closed magnetic field line boundary during
613 balanced dayside and nightside reconnection, *Ann. Geophys.*, 20, 1617-1630,
614 <https://doi.org/10.5194/angeo-20-1617-2002>, 2002.

615 Prikryl, P., Jayachandran, P. T., Chadwick, R., and Kelly, T. D.: Climatology of GPS phase
616 scintillation at northern high latitudes for the period from 2008 to 2013, *Ann. Geophys.*, 33,
617 531-545, <https://doi.org/10.5194/angeo-33-531-2015>, 2015.

618 Pryse, S. E., Wood, A.G., Middleton, H. R., McCrea, I. W., and Lester, M.: Reconfiguration of
619 polar cap plasma in the magnetic midnight sector, *Ann. Geophys.*, 24, 2201-2208,
620 <https://doi.org/10.5194/angeo-24-2201-2006>, 2006.

621 Pryse S. E., Kersley, L., and Russell C. D.: Scintillation near the F layer trough over northern
622 Europe, *Radio Science* 26, 4, 1105-1114, <https://doi.org/10.1029/91RS00490>, 1991.

623 Rideout, W. and Coster, A. J.: Automated GPS processing for global total electron content
624 data, *GPS Solutions*, 10, 219-228, <https://doi.org/10.1007/s10291-006-0029-5>, 2006.

625 Rino, C. L., Livingston, R. C., Tsunoda, R. T., Robinson, R. M., Vickrey, J. F., Senior, C., Cousins,
626 M. D., Owen, J., and Klobuchar, J. A.: Recent studies of the structure and morphology of
627 auroral-zone F-region irregularities, *Radio Sci.*, 18, 1167-1180, 10.1029/RS018i006p01167,
628 1983.

629 Rodger, A. S., Pinnock, M., Dudeney, J. R., Baker, K. B., and Greenwald, R. A.: A new
630 mechanism for polar patch formation, *J. Geophys. Res.*, 99, 6425-6436,
631 doi:10.1029/93JA01501, 1994.

632 Ruohoniemi, J. M., and Greenwald, R. A.: Dependencies of high- latitude plasma convection:
633 Consideration of interplanetary magnetic field, seasonal, and universal time factors in
634 statistical patterns, *J. Geophys. Res.*, 110, A09204, doi:10.1029/2004JA010815, 2005.

635 Smith, A. M., Mitchell, C. N., Watson, R. J., Meggs, R. W., Kintner, P. M., Kauristie, K., and
636 Honary, F.: GPS scintillation in the high arctic associated with an auroral arc, *Space Weather*,
637 6, S03D01, doi:10.1029/2007SW000349, 2008.

638 Sojka, J., Bowline, M., Schunk, R., Decker, D., Valladares, C., Sheehan, R., Anderson, D., and
639 Heelis, R.: Modeling Polar Cap F-Region Patches Using Time Varying Convection, *Geophys.*
640 *Res. Lett.*, 20, 1783-1786, Doi:10.1029/93gl01347, 1993.

641 Spogli, L., Alfonsi, L., De Franceschi, G., Romano, V., Aquino, M. H. O., and Dodson, A.:
642 Climatology of GPS ionospheric scintillations over high and mid-latitude European regions,
643 *Ann. Geophys.*, 27, 3429-3437, <https://doi.org/10.5194/angeo-27-3429-2009>, 2009.

644 Thomas, E. G., and Shepherd, S. G.: Statistical patterns of ionospheric convection derived from
645 mid-latitude, high-latitude, and polar SuperDARN HF radar observations, *J. Geophys. Res.*,
646 123, 3196–3216, <https://doi.org/10.1002/2018JA025280>, 2018.

647 Tsunoda, R. T.: High-latitude F region irregularities: A review and synthesis, *Rev. Geophys.*,
648 26, 719-760, <https://doi.org/10.1029/RG026i004p00719>, 1988.

649 Valladares, C. E., Decker, D. T., Sheehan, R., Anderson, D. N., Bullett, T. and Reinisch, B. W.:
650 Formation of polar cap patches associated with north-to-south transitions of the
651 interplanetary magnetic field, *J. Geophys. Res.*, 103, 14657-14670,
652 <https://doi.org/10.1029/97JA03682>, 1998.

653 Valladares, C.E., Basu, S., Buchau, J., and Friis-Christensen, E.: Experimental evidence for the
654 formation and entry of patches into the polar cap, *Radio Sci.*, 29, 167-194, doi:
655 10.1029/93RS01579, 1994.

656 van der Meeren, C., Oksavik, K., Lorentzen, D., Moen, J. I., and Romano, V.: GPS scintillation
657 and irregularities at the front of an ionization tongue in the night-side polar ionosphere, *J.*
658 *Geophys. Res. Space Physics*, 119, 8624–8636, doi:10.1002/2014JA020114, 2014.

659 van der Meeren, C., Oksavik, K., Lorentzen, D. A., Rietveld, M. T., and Clausen, L. B. N.: Severe
660 and localized GNSS scintillation at the poleward edge of the nightside auroral oval during
661 intense substorm aurora, *J. Geophys. Res. Space Physics*, 120, 10,607–10,621,
662 doi:10.1002/2015JA021819, 2015.

663 van der Meeren, C., Oksavik, K., Lorentzen, D. A., Paxton, L. J., and Clausen, L. B. N.: Scintillation
664 and irregularities from the nightside part of a Sun-aligned polar cap arc, *J. Geophys. Res. Space*
665 *Physics*, 121, 5723–5736, doi:10.1002/2016JA022708, 2016.

666 Vierinen, J., Coster, A. J., Rideout, W. C., Erickson, P. J., and Norberg, J.: Statistical framework
667 for estimating GNSS bias, *Atmos. Meas. Tech. Discuss.*, 8, 9373–9398, doi:10.5194/amtd-8-
668 9373-2015, 2015.

669 [Wang, Y., Zhang, Q. - H., Jayachandran, P. T., Moen, J., Xing, Z. - Y., Chadwick, R., et al. \(2018\).](#)
670 [Experimental evidence on the dependence of the standard GPS phase scintillation index on](#)
671 [the ionospheric plasma drift around noon sector of the polar ionosphere. *Journal of*](#)
672 [*Geophysical Research: Space Physics*, 123, 2370–2378.](#)
673 [<https://doi.org/10.1002/2017JA024805>](#)

674 Wannberg, G., Wolf, I., Vanhainen, L.-G., Koskeniemi, K., Röttger, J., Postila, M., Markkanen,
675 J. Jacobsen, R., Stenber, A., Larsen, R., Eliassen, S., Heck, S., and Huuskonen, A.: The EISCAT

676 Svalbard radar: A case study in modern incoherent scatter radar system design, *Radio Sci.*, 32,
677 2283–2308, doi:10.1029/97RS01803, 1997.

678 Walker, I. K., Moen, J., Kersley, L., and Lorentzen, D. A.: On the possible role of cusp/cleft
679 precipitation in the formation of polar-cap patches, *Ann. Geophys.*, 17, 1298-1305,
680 doi.org/10.1007/s00585-999-1298-4, 1999.

681 Weber, E., Buchau, J., Moore, J., Sharber, J., Livingston, R., Winningham, J., and Reinisch, B.:
682 F-layer ionization patches in the polar cap, *J. Geophys. Res.*, 89, 1683,
683 doi:10.1029/Ja089ia03p01683, 1984

684 Zwickl, R. D., Doggett, K.A., Sahm, S., Barrett, W.P., Grubb, R.N., Detman, T.R., Raben, V.J.,
685 Smith, C.W., Riley, P., Gold, R.E., Mewaldt, R.A., Maruyama T.: The NOAA Real-Time Solar-
686 Wind (RTSW) system using ACE data, *Space Sci. Rev.*, 86, 633–648, doi:10.1023/
687 A:1005044300738, 1998.